Available online at https://link.springer.com/journal/42241
http://www.jhydrodynamics.com
Journal of Hydrodynamics, 2022
https://doi.org/10.1007/s42241-022-0035-2

Preliminary control of the air entrainment in bow wave based on the Liutex force method

Yi-ding Hu[1], Jian-wei Wu[2], De-cheng Wan[1*], Guo Wang[3], Yi-qian Wang[4]
1. *Computational Marine Hydrodynamics Lab (CMHL), School of Naval Architecture, Ocean and Civil Engineering, Shanghai Jiao Tong University, Shanghai 200240, China*
2. *Wuhan Second Ship Design and Research Institute, Wuhan 430205, China*
3. *Marine Design and Research Institute of China, Shanghai 200011, China*
4. S*chool of Mathematical Science, Soochow University, Suzhou 215006, China*

(Received December 24, 2021, Revised April 5, 2022, Accepted April 6, 2022, Published online June 23, 2022)

Abstract: Trails induced by air entrainment of bow wave breaking can be observed clearly around an advancing ship, making it prong to be detected and causing reduction in hydrodynamic performance. In breaking bow wave region, different scale of coherent vortex structures related closely to the air entrainment are generated. The formation and evolution of bubble clouds can be accounted partly by the swirling vortex flow of the jet plunging. In this work, high-fidelity simulation of the bow wave breaking around a rectangular thin plate is performed with the in-house code BAMR-SJTU. A Liutex force model is constructed to investigate the interaction between the free surface and vortices, and to explore the possibility of alleviating or controlling the air entrainment. This study is the first attempt to manipulate vortices corresponding to the air entrainment of the bow wave breaking. Some typical vortex structures based on the Liutex vortex identification method and the distribution of the vortex force are presented. Comparison of the vortex structures and the entrapped bubbles is conducted to illustrate the efficiency of Liutex force model in air entrainment control.

Key words: Bow wave breaking, air entrainment, coherent vortex structures, Liutex force field model

Introduction

Bow wave breaking generated by ship advancing in calm water contains complex physical processes and may have significant influences on hydrodynamic performance. Because of wave plunging, a large amount of air is entrapped into the wake, lasting for a long distance downstream. These bubbly flows have significant optical and acoustic characteristics which make the ships exposed to the remote sensing and sonar detections. Therefore, it is necessary to study the generation of the bubbles in the wake region and some measures should be taken to alleviate and control the occurrence of the entrained air.

At the early stage, owing to the limitation of numerical methods and computation capacity, model experiments were conducted to study the dynamic of bow wave breaking. To identify the dependence of wave profiles on bow shapes, a series of experiments are performed by placing a deflecting plate (with different water entrance angles and heel angles) in a supercritical free-surface flow[1-3]. Detailed study of the flow field within breaking waves generated by a ship hull was made by Dong et al.[4]. And Roth et al.[5], Olivieri et al.[6] emphasized the phenomena of "scars" that may abruptly change the surface elevation forming streamwise streaks, and performed statistical analysis of the wave pattern in detail. These studies often utilized particle image velocimetry (PIV), high-speed photography and tracer particle to obtain a general flow dynamic. In the present study, we focus on the air entrainment of the bow wave breaking and explore the possibility of using the vortex force model to alleviate air entrainment.

Swirling vortex plays an important role in the generation of the bubbles which may be entrained by fragmenting the surface with strong shear stress. There are plenty of researches concerning the relations between vortices structure and air entrainment. An experiment is performed by Takahashi et al.[7] to investigate the onset conditions of air entrainment by

Project supported by the National Key Research and Development Program of China (Grant No. 2019YFB1704200), the National Natural Science Foundation of China (Grant Nos. 51879159, 52131102).
Biography: Yi-ding Hu (1998-), Male, Ph. D. Candidate
E-mail: huyiding@sjtu.edu.cn
Corresponding author: De-cheng Wan
E-mail: dcwan@sjtu.edu.cn

a single vortex and summarized three typical types of air entrainment mechanisms. The interaction between the free surface and a heterotrophic vortex pair is investigated to describe the characteristics of 3-D flow structures (scars and striations) by Sarpkaya and Suthon[8]. Ezure et al.[9] studied transient behaviors of air entrainment and found that the extension of the air core length delay the increase of circulation around the vortex. Free surface deformation before entrainment due to a vortex in Stokes flow is studied analytically by Jeong[10]. Recent studies by André and Bardet[11] investigated air entrainment in the relaxation of a horizontal shear layer below a free surface and two air entrainment mechanisms driven by vortex instability are reported. Previous researchers mainly show the relations between vortex structures and air entrainment in a relatively simple situation, and few studies consider the air entrainment due to vortices in bow wave breaking. The interaction between the free surface and the vortices in bow wave breaking is investigated numerically in the present work.

In the past few decades, a number of vortex identification methods have been developed. According to Liu et al.[12], the vortex identification methods can be divided into three generations. The first generation methods are based on vorticity and have difficulty in identifying vortex structures especially in the near wall region. The second generation methods were proposed to overcome this issue, including Q, λ_2, Δ, λ_{ci} and other methods[13-16]. However, it is difficult to determine the threshold and identify vortex from pure shear flows for these methods. In recent years, the third generation methods have been proposed by Liu et al.[17] to overcome the shear contamination issue with the Liutex vector to represent the rigid rotation part of fluid motion. Its magnitude that represents the rotational strength of the fluid rotation is twice the angular velocity of rigid rotation and direction is consistent with the rotational axis. The Liutex system can provide the full six core elements[18] of vortex identification including absolute strength, relative strength, local rotational axis, vortex rotation axis, vortex core size and vortex boundary. Many methods such as Liutex magnitude iso-surface[19], Liutex-Omega method[20] and Liutex core line method[21], etc. have been proposed to visualize vortices.

A preliminary study of vortex force model based on the Liutex method is conducted by Yu and Wang[22] and two vortex control models are proposed, namely the centripetal force field model and the counter-rotation force field model to manipulate vortices and obtain vortex dynamics numerically. The Liutex-based vortex force model is introduced in a cavitation flow problem of a 2-D Clark-Y hydrofoil, and a cavitation suppression method is proposed by Wang et al.[23] accordingly. Recently, the influence of the Liutex force on the drag and lift forces, as well as the flow field of uniform flow past a stationary cylinder problem is studied by Zhao et al.[24].

The object of this paper is to simulate ship bow waves accurately and consider the influence of the coherent vortex structures on the air entrainment of the bow wave breaking. The newly introduced vortex definition and identification system of Liutex is implemented in BAMR-SJTU solver. Some typical vortex stuctures are shown with the Liutex identification method. The Liutex-based force model is used to manipulate the vortex structures to alleviate the air entrainment. Some preliminary conclusions are reported.

1. Computational methods

1.1 *Governing equations and Liutex force field model*

Governing equations for two-phase flow problems contain the continuity equation and the momentum equation which are written as

$$\frac{\partial \rho}{\partial t} + \nabla \cdot (\rho \boldsymbol{u}) = 0 \tag{1}$$

$$\frac{\partial \rho \boldsymbol{u}}{\partial t} + \nabla \cdot (\rho \boldsymbol{u}\boldsymbol{u}) = -\nabla p + \nabla \cdot (\mu \boldsymbol{S}) + \rho \boldsymbol{g} + \sigma \kappa \delta \boldsymbol{n} \tag{2}$$

where ρ and $\boldsymbol{u}$ represent density and the velocity vector respectively, p is pressure of the fluid, μ represents dynamic viscosity, $\boldsymbol{S}$ is the rate of strain tensor, $\boldsymbol{g}$ indicates gravitational acceleration. The surface tension which is non-zero only at the location of the interface is considered. σ is the surface tension coefficient, κ is the interfacial curvature which can be estimated by the volume fraction field, δ is the Dirac delta function and $\boldsymbol{n}$ is interface unit normal.

The interface transport equation is given by

$$\frac{\partial C}{\partial t} + \boldsymbol{u} \cdot (\nabla C) = 0 \tag{3}$$

C is defined as the volume fraction in a cell with its value in between zero and one. Zero and one represent air and liquid respectively. The density ρ and viscosity μ in Eqs. (1), (2) are computed using the volume fraction in Eqs. (4), (5).

$$\rho = C\rho_l + (1 - C)\rho_g \tag{4}$$

$$\mu = C\mu_l + (1-C)\mu_g \tag{5}$$

where l and g represent the fluid and liquid phase, respectively.

Two different strategies are provided by Yu and Wang[22] to control the flow field. One is the centripetal force model, another is the counter-rotation force model. As a preliminary study, only the centripetal force model is considered, the expression is given as

$$\boldsymbol{a} = \frac{\boldsymbol{R}}{2} \times \left(\frac{\boldsymbol{R}}{2} \times \boldsymbol{l} \right) = \frac{1}{4} \boldsymbol{R} \times (\boldsymbol{R} \times \boldsymbol{l}) \tag{6}$$

$\boldsymbol{R}$ is the Liutex vector, an explicit expression which is derived by Xu et al.[25]

$$\boldsymbol{R} = R\boldsymbol{r} = \left[\boldsymbol{\omega} \cdot \boldsymbol{r} - \sqrt{(\boldsymbol{\omega} \cdot \boldsymbol{r})^2 - 4\lambda_{ci}^2} \right] \boldsymbol{r} \tag{7}$$

where $\boldsymbol{R}$ is the magnitude of Liutex vector, $\boldsymbol{\omega}$ is the vorticity vector, $\boldsymbol{r}$ is the real eigenvector and λ_{ci} is the imaginary part of the complex eigenvalue.

$\boldsymbol{l}$ in Eq. (6) is a rotation vector defined starting at any field point P and ending at the vortex core centre point P_o. P_o indicates the local minimum pressure point. In this study, $\boldsymbol{l}$ is simplified to Eq. (8) that is consistent with Zhao et al.[24].

$$\boldsymbol{l} = \frac{\boldsymbol{u}}{\Delta \boldsymbol{u}} \tag{8}$$

Then we add the source term to the right of the momentum equation, and the modified equation is expressed as

$$\frac{\partial \rho \boldsymbol{u}}{\partial t} + \nabla \cdot (\rho \boldsymbol{u}\boldsymbol{u}) = -\nabla p + \nabla \cdot (\mu \boldsymbol{S}) + \rho \boldsymbol{g} + \sigma \kappa \delta \boldsymbol{n}_\sigma \pm c\boldsymbol{a} \tag{9}$$

The solution procedures are described as follows: when the flow field developed to a statistically stable state, ($t = 2$ s for the present simulation), the Liutex force vector and corresponding centripetal acceleration is computed at the current time step. Afterwards, the centripetal force is added to the Navier-Stokes equation as shown in Eq. (9) to update the flow field for the subsequent time step. The parameter c is used to control the magnitude of the added force field.

1.2 *Numerical methods*

In order to resolve the free surface accurately, the block-based adaptive mesh refinement (BAMR) strategy[26] is used. By this method, the local resolution can be improved while ensuring the computational efficiency. In BAMR, blocks are taken as the basic manipulation units for parallel loading balance and all the blocks have identical logical structure, which is highly applicable for performing massively parallel computations and implementing high-order schemes.

Formation and evolution of bow waves show strongly nonlinear features with large deformation, which is challenging for the present simulation. A coupled level set and volume-of-fluid (CLSVOF)[27] interface capturing method which combines the advantages of level set method and volume-of-fluid method are adopted to compute moving interface. In the CLSVOF, the interface is reconstructed linearly via the VOF function and the interface normal vector is computed from the level set function. Based on the reconstructed interface, the level set functions are re-distanced via geometric computation to maintain mass conservation.

An efficient immersed boundary method proposed by Liu and Hu[28] was adopted to handle the rectangular flat immersed in fluid. One of the benefits is that the treatment of boundary conditions of the body surface can be simplified, thus the algorithm based on Cartesian grid solver can be implemented straightforwardly. Specifically, a forcing term is added to the right-hand side of the Navier-Stokes equation to represent the influence of the body. The forcing term should be reconstructed in each computational step by using boundary conditions and velocity field near the body surface. Position of body surface is identified implicitly by the signed distance function. Since the grid boundaries are not necessarily to conform to the boundary of the immersed body, mesh generation can be greatly simplified.

2. Simulation of the bow wave breaking

2.1 *Numerical set-up*

In this sub-section, the typical vortex structures are presented based on the Liutex vortex identification method and the constructed Liutex force model is applied to control air entrainment in bow wave.

The simulation in this study is performed with a rectangular flat plate of length 0.782 m, height 0.5 m, immersed at a draught 0.2 m, a constant heel angle (angle between the plate and the vertical axis) $\gamma = 10°$ and the water entrance angles (angle between the plate and flow direction) $\theta_E = 45°$. The incoming speed U is 1.75 m/s and the draft Froude number is 1.25. The computation is carried out in 3-D domain

[−0.5 m,1.3 m], [−0.3 m,1.5 m] and [−0.8 m,1.0 m] in the X, Y and Z directions. The length of the longitudinal, transverse, and vertical dimensions is equal to 1.8 m. The origin of coordinate is located at the intersect point between initial undisturbed interface and the front of the rectangular plate. The arrangement of numerical simulation is shown in Fig. 1. Some results of numerical simulation agree well with the experimental measurements and theoretical results[29] with relative coarse meshes which indicates the accuracy of the numerical approaches.

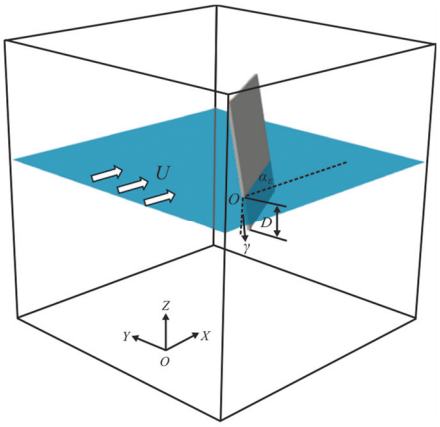

Fig. 1 (Color online) Sketch to demonstrate configuration of the computational domain and numerical setups of the plate

In the present simulation, the refinement level is from 2 to 7 and the minimum grid spacing is 0.002 m. 200 physical cores (Intel Xeon E5-4627, 3.4 GHz) are used for parallel computation and the peak gird number is about 68.4×10^6. Figure 2(a) shows the BAMR blocks used for simulation, each block is filled by 8×8×8 uniform grids of different levels, Fig. 2(b) shows local instantaneous iso-surface with the highest refinement level.

2.2 *Air entrainment*

Figure 3 shows the violent free surface region in the wave breaking. The bow wave breaking involves very complex air entrainment phenomenon owing to the mass and momentum exchanges taking place at the free surface. As shown in Fig. 3, large amount of air is entrained due to the breaking bow wave. Two long visible bubbly trails are observed below the shoulder wave and mixed in the turbulent flow generated by the trailing edge of plate, by which the main characteristic of the common "white water/foam" can be explained. These wakes usually last for a long time during the wave breaking and dissipate to a large range of downstream, leaving obvious streaks. The experiment done by Olivieri et al.[6] suggests that these strikes are the result of counter-rotating vortex pairs generated by the breaking bow waves. So it is essential to understand the mechanism of air entrainment due to the rotating vortex beneath the free surface.

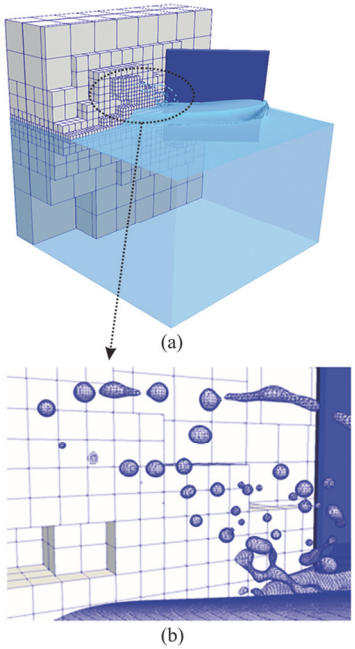

Fig. 2 (Color online) (a) BAMR blocks of the computational domain, each block contains 8×8×8 uniform mesh, (b) Local instantaneous iso-surface with the highest refinement level

Fig. 3 (Color online) Long bubbly wakes behind the plat (flow field is rendered with ray tracing technique)

There are two reasons leading to the formation of bubble clusters beneath the free surface in the wake, one is the collapse of the cavity behind the plate and another is the interaction between the free surface and vortices. As shown in Fig. 4, a large amount of air is entrapped and a large air pocket is formed in the bow wave breaking. The rotation of the air pocket yields coherent vortex structures around it. Vortices driven the motion of air cavity, including the entraining, accumulating, merging and stretching of bubbles. The interaction between bubbles and vortices also leads to

the breakup of bubbles which produces the typical bubble clusters containing bubbles of different scales as shown in Fig. 4.

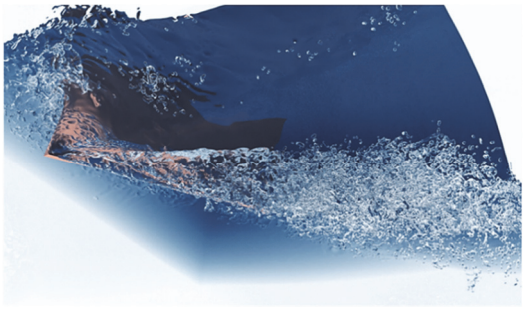

Fig. 4 (Color online) Underwater viewpoint of the bubble clusters below the free surface

2.3 *Typical vortex structures in bow wave breaking*

For better demonstration of the underlying flow physics of vortex interacting with free surface, a sketch is given (Fig. 5). Different scales of coherent vortex structures related closely to the air entrainment are contained in the bow wave breaking. Free surface fluctuations also can be accounted for partially by the presence of vortices. When the vortices have enough kinetic energy to overcome the potential energy of gravity and surface tension, wave breaking will be trigged, leading to air entrainment eventually.

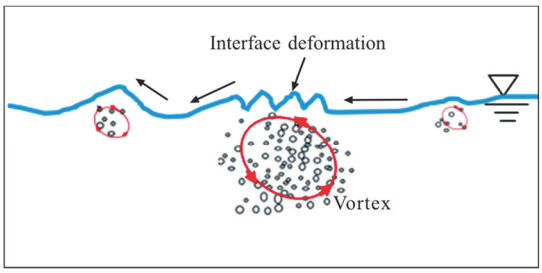

Fig. 5 (Color online) Sketch to illustrate the interference between vortex and the air entrainment

In bow wave breaking, coherent vortex structures in the vicinity of the free surface will result in the occurrence of air entrainment. The coherent vortex structures below the interface identified using the Liutex identification method are shown in Fig. 6. From the figure, we can find that these vortex structures are primarily located in the area where bubbles are generated. It suggests the generation of bubbles is correlated with the vortex structure. The vortex structures are mainly induced by the first impact and the successive splash-ups of the bow wave breaking. As the vortex approaches the free surface, it induces large surface distortion which leads to the formation of the air tube connecting to the free surface. As the flow develops, the air cavity breaks up into bubbles. The flow between the vortices creates a depression in the surface, which appears as a scar.

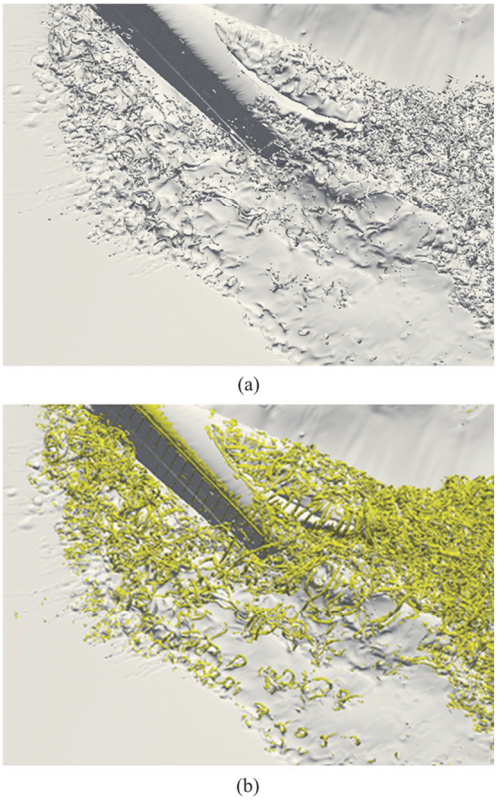

Fig. 6 (Color online) (a) Distribution of the bubbles underwater (top view), (b) Typical vortex structures based on the Liutex vortex identification method underneath the surface

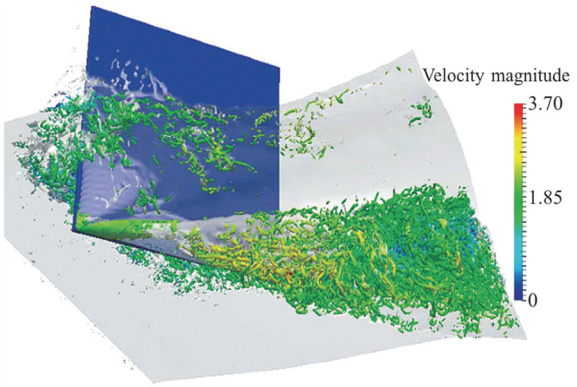

Fig. 7 (Color online) Vortex structures wrapped around the air cavity

Figure 7 reveals the complicated vortex structures wrapped around the air cavity owing to the rotating cavity. The wake region exhibits large-scale vortex structures and massive air entrainment. These coherent turbulent structures have a significant influence on bubble generation under strong shear motion. The wake vortex structures also intensify the breakup and transport of the bubble cluster.

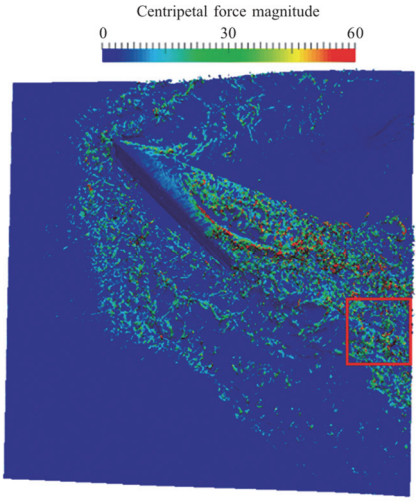

Fig. 8 (Color online) Distribution of the Liutex-based force filed underwater

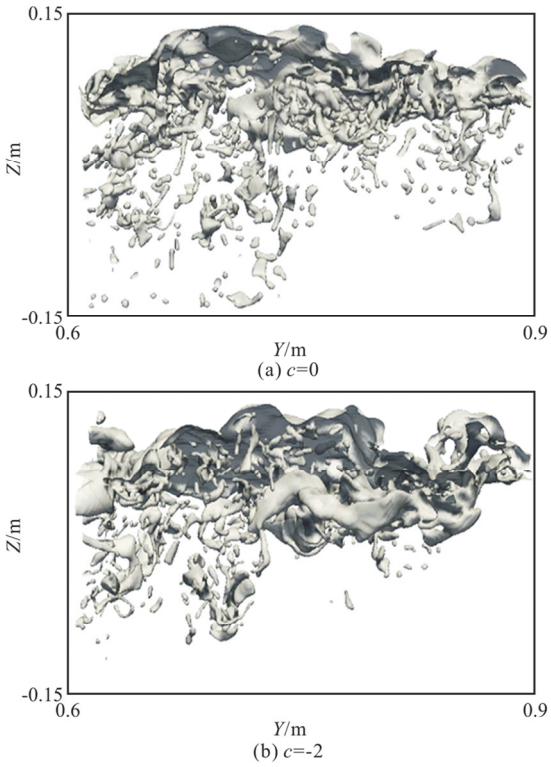

Fig. 9 The local air entrainment in the wake of bow wave breaking with different c values ($t = 2.05$s)

2.4 *Centripetal force model*

Few efficient methods are developed to control air entrainment despite it is important for the hydrodynamic performance of floating body. In this part, the possibility of alleviating the air entrainment based on the Liutex force model is discussed. The vortex structures in the wave breaking are manipulated and the response of the flow field with the control of the vortex force is investigated. According to Eq. (6), the distribution of the Liutex-based force field underwater is given in Fig. 8. We found that the vortex force is distributed where the vortex structures exist, in the wake region where the force magnitude is relatively larger.

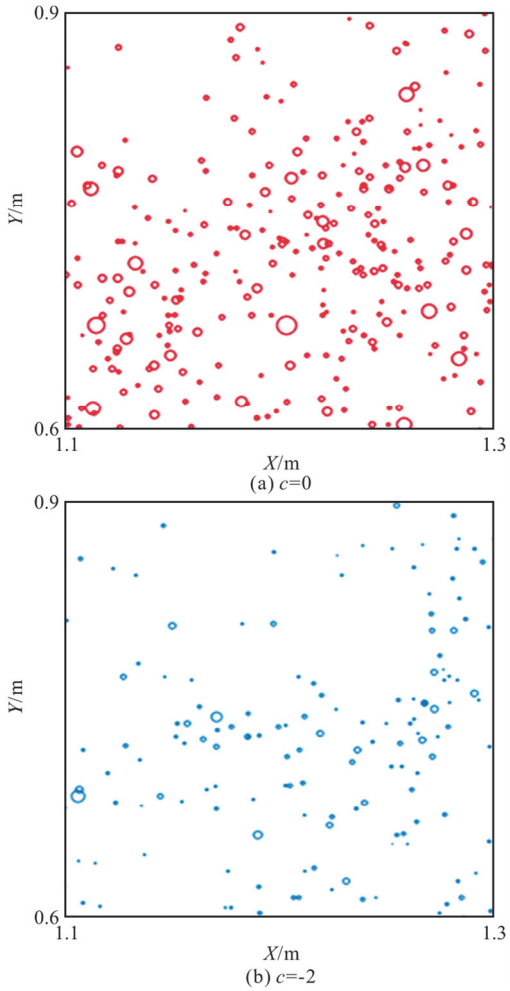

Fig. 10 (Color online) Local bubble distributions with different c values (magnified 20 times)

Due to the intricate complexity of the whole system, we now focus on the local air entrainment in the wake of bow wave breaking that circumscribed by red square as shown in Fig. 8, in the region of $X \in [1.1\,\text{m}, 1.3\,\text{m}]$, $Y \in [0.6\,\text{m}, 0.9\,\text{m}]$ and $Z \in [-0.15\,\text{m}, 0.15\,\text{m}]$. It is noted that at $t = 2$ s, the flow field reachs a statistically stable state, and the centripetal forces begin to take effect, with the whole computational domain exerted by the Liutex force model. Results of the case $(c = 0)$ with no contribution of Liutex force and the case $(c = -2)$ with subtracting the centripetal force are obtained at $t = 2.05$ s which are shown in Fig. 9. It is observed

that the case of $c = 0$ entrains relatively more bubbles than the case with the Liutex force model ($c = -2$). It can be concluded that air entrainment is alleviated under the vortex force.

In order to see the distribution of underwater bubbles more clearly, the bubbles are represented by the equivalent-radius-circles, as shown in Fig. 10. For demonstration, the size of bubbles is magnified 20 times. We can see the bubbles size distribution clearly with different c values. When the flow field is subtracted the centripetal force, the bubble count and size are reduced significantly. On the other hand, we also notice that bubbles of larger radius are much less than the controlled case, which indicates the vortex forces have a significant effect on generation of large bubbles. This may be explained by the large-scale vortex structure adjacent to large bubble, where the corresponding Liutex force model is also relatively large.

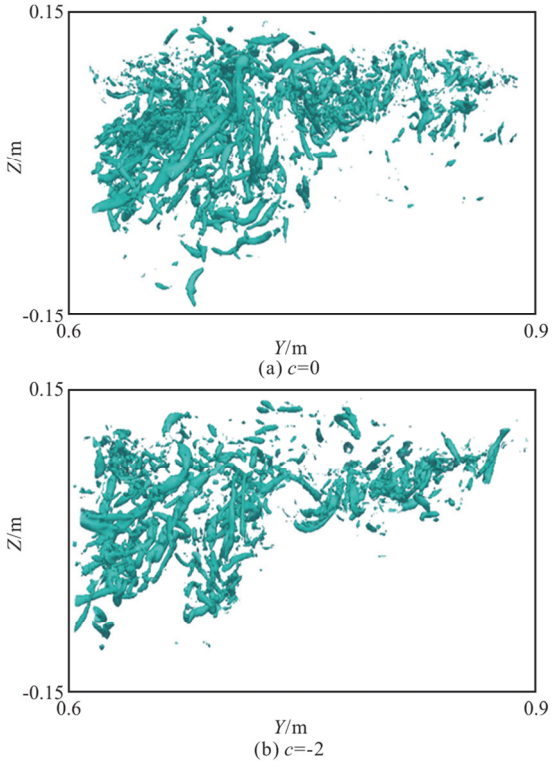

Fig. 11 (Color online) Comparison of the vortex structures between different c values

The vortex structures around the bubble at the local region are shown in Fig. 11 for comparison. Similar conclusions can be drawn for vortex structures. Clearly, compared with the case of $c = 0$, the vortex structures after exerting the Liutex force model become more scattered. It indicates that some vortex structures are weakened or cancelled out by subtracting the centripetal force.

3. Conclusion

A preliminary study of air entrainment of bow wave based on the Liutex force model is presented in this paper. The interaction between the free surface and vortices is investigated. Following conclusions can be drawn: (1) The generation of bubbles is correlated with vortices. (2) Owing to the presence of highly vortices at free surface, a large number of bubbles are entrapped in the bow wave breaking. (3) Vortex structures are weakened by exerting the Liutex force model. (4) Liutex-based vortex dynamics can control flow field efficiently and alleviate air entrainment. In the present study, the Liutex-based vortex dynamics are used only to investigate the distribution of the entrapped bubbles. More characteristics of the entrapped bubbles due to the vortices will be explored in the future.

References

[1] Waniewski T. A., Brennen C. E., Raichlen F. Experimental simulation of a bow wave [C]. *ASME Fluids Engineering Division Summer Meeting*, Vancouver, Canada, 1997.

[2] Waniewski T. A., Brennen C. E., Raichlen F. Measurements of air entrainment by bow waves [J]. *Journal of Fluids Engineering*, 2001, 123(1): 57-63.

[3] Waniewski T. A., Brennen C. E., Raichlen F. Bow wave dynamics [J]. *Journal of Ship Research*, 2002, 46(1): 1-15.

[4] Dong R. R., Katz J., Huang T. T. On the structure of bow waves on a ship model [J]. *Journal of Fluid Mechanics*, 1997, 346: 77-115.

[5] Roth G. I., Mascenik D. T., Katz J. Measurements of the flow structure and turbulence within a ship bow wave [J]. *Physics of Fluids,* 1999, 11(11): 3512-3523.

[6] Olivieri A., Pistani F., Wilson R. et al. Scars and vortices induced by ship bow and shoulder wave breaking [J]. *Journal of Fluids Engineering*, 2007, 129(11): 1445-1459.

[7] Takahashi M., Inoue A., Aritomi M. et al. Gas entrainment at free surface of liquid, (II) Onset conditions of vortex-induced entrainment [J]. *Journal of Nuclear Science and Technology*, 1988, 25(3): 245-253.

[8] Sarpkaya T., Suthon P. Interaction of a vortex couple with a free surface [J]. *Experiments in Fluids*, 1991, 11(4): 205-217.

[9] Ezure T., Kimura N., Hayashi K. et al. Transient behavior of gas entrainment caused by surface vortex [J]. *Heat Transfer Engineering*, 2008, 29(8): 659-666.

[10] Jeong J. T. Free-surface deformation due to spiral flow owing to a source/sink and a vortex in Stokes flow [J]. *Theoretical and Computational Fluid Dynamics*, 2012, 26(1): 93-103.

[11] André M. A., Bardet P. M. Free surface over a horizontal shear layer: Vorticity generation and air entrainment mechanisms [J]. *Journal of Fluid Mechanics*, 2017, 813: 1007-1044.

[12] Liu C., Gao Y. S., Dong X. R. et al. Third generation of vortex identification methods: Omega and Liutex/Rortex based systems [J]. *Journal of Hydrodynamics,* 2019, 31(2): 205-223.

[13] Hunt J., Wray A., Moin P. Eddies, streams, and convergence zones in turbulent flows [R]. Proceedings of the Summer Program. Center for Turbulence Research, 1988, 193-208.
[14] Jeong J., Hussain F. On the identification of a vortex [J]. *Journal of Fluid Mechanics*, 1995, 285: 69-94.
[15] Chong M. S., Perry A. E., Cantwell B. J. A general classification of three-dimensional flow fields [J]. *Physics of Fluids*, 1990, 2(5): 765-777.
[16] Zhou J., Adrian R., Balachandar S. et al. Mechanisms for generating coherent packets of hairpin vortices in channel flow [J]. *Journal of Fluid Mechanics*, 1999, 387: 252-296.
[17] Liu C., Gao Y., Tian S. et al. Rortex-A new vortex vector definition and vorticity tensor and vector decompositions [J]. *Physics of Fluids*, 2018, 30(3): 035103.
[18] Liu C., Wang Y. Q. Liutex and third generation of vortex definition and identification [M]. Cham, Switzerland: Springer International Publishing, 2021.
[19] Liu J., Gao Y., Liu C. An objective version of the Rortex vector for vortex identification [J]. *Physics of Fluids*, 2019, 31(6): 065112.
[20] Dong X., Gao Y., Liu C. New normalized Rortex/vortex identification method [J]. *Physics of Fluids*, 2019, 31(1): 011701.
[21] Gao Y. S., Liu J. M., Yu Y. et al. A Liutex based definition of vortex rotation axis line [J]. *Journal of Hydrodynamics*, 2019, 31(3): 445-454.
[22] Yu H. D., Wang Y. Q. Liutex-based vortex dynamics: A preliminary study [J]. *Journal of Hydrodynamics*, 2020, 32(6): 1217-1220.
[23] Wang Y. Q., Yu H. D., Zhao W. W. et al. Liutex-based vortex control with implications for cavitation suppression [J] *Journal of Hydrodynamics*, 2021, 33(1): 74-85.
[24] Zhao W. W., Wang Y. Q., Wan D. C. Parametric study of Liutex-based force field models [J]. *Journal of Hydrodynamics,* 2021, 33(1): 86-92.
[25] Xu W., Gao Y., Deng Y. et al. An explicit expression for the calculation of the Rortex vector [J]. *Physics of Fluids*, 2019, 31(9): 095102.
[26] Liu C., Hu C. Block-based adaptive mesh refinement for fluid structure interactions in incompressible flows [J]. *Computer Physics Communications*, 2018, 232: 104-123.
[27] Sussman M., Puckett E. G. A coupled level set and volume-of-fluid method for computing 3D and axisymmetric incompressible two-phase flows [J]. *Journal of Computational Physics*, 2000, 162(2): 301-337.
[28] Liu C., Hu C. An efficient immersed boundary treatment for complex moving object [J]. *Journal of Computational Physics*, 2014, 274: 654-680.
[29] Hu Y. D., Liu C., Wan D. C. Numerical simulation of bow waves generated by a rectangular plate [C]. *Proceeding the Thirtieth (2020) International Ocean and Polar Engineering Conference*, Shanghai, China, 2020, 3515-3520.